Thermochemical non-equilibrium effects on passive control of hypersonic boundary-layer transition using regular porous coating

Xiaowen Wang* and Xiaolin Zhong #1
Mechanical and Aerospace Engineering Department
University of California, Los Angeles, CA 90095

Abstract

In the past decade, passive control of hypersonic boundary-layer transition using porous coatings has been studied by theoretical analyses, experiments, and numerical simulations. It was found that porous coating significantly stabilizes Mack's second mode and slightly destabilizes Mack's first mode. However, there is only quite limited studies on the stabilization efficiency of porous coating. And no work has been reported about the thermochemical non-equilibrium effects of hypersonic flows on the stabilization efficiency. In this paper, we conduct numerical simulations on the passive control of hypersonic boundary-layer transition using regular porous coating. The stabilization of a Mach 5.92 flat-plate boundary layer is first studied for perfect gas flow. The results show that, at approximately the same porosity, regular coating is weaker in first-mode destabilization and second-mode stabilization than felt-metal coating. The porosity decrease of regular coating leads to even weaker first-mode destabilization and second-mode stabilization. The results also show that the first-mode destabilization decreases as the phase angle of admittance decreases and the thermochemical non-equilibrium of hypersonic flows may affect the stabilization efficiency of regular coating. Therefore, numerical simulations based on perfect gas flow may not be enough. The effects of thermochemical non-equilibrium flow including internal energy excitations, translation-vibration energy relaxation, and chemical reactions among different species need to be considered. We have developed a new high-order shock-fitting solver for non-equilibrium flow simulations based on the 5-species air chemistry and recently thermal non-equilibrium models. The code package has been tested and is being applied to numerical simulation of a Mach 12.56 boundary layer over a blunted wedge of a half angle 20 degree. Thermochemical non-equilibrium effects of hypersonic flows on the steady base flow is investigated by comparing numerical results of perfect gas flows and thermochemical non-equilibrium flow. Unsteady simulations on the passive control of hypersonic non-equilibrium boundary-layer transition using regular porous coating are currently ongoing.

1. Introduction

The performance of hypersonic transportation vehicles and re-entry vehicles and the design of their thermal protection systems are significantly affected by the laminar-turbulent transition of boundary-layer flows over vehicle surfaces, because a turbulent boundary layer generates much higher drag and surface heating than a laminar one. Transition can have a first-order impact on the lift, drag, stability, control, and heat transfer properties of the vehicles [1]. Transition control to maintain laminar boundary-layer flows or delay transition can result in lower drag, lower surface heating, and higher fuel efficiency.

In order to predict and control boundary-layer transition, extensive studies have been carried out

* Research Associate, Mechanical and Aerospace Engineering Department, UCLA, AIAA Senior Member
# Professor, Mechanical and Aerospace Engineering Department, UCLA, AIAA Associate Fellow

focusing on transition mechanisms [2]. It has been demonstrated that the transition of external shear flows, including boundary layers, strongly depends on the amplitude of environmental disturbance [3]. Figure 1 schematically shows paths of external shear flow transition. For small amplitude disturbance, the transition of a boundary layer over a smooth surface generally consists of the following three stages: 1. receptivity process during which environmental disturbances enter the boundary layer and excite boundary-layer waves. 2. Modal growth of unstable boundary-layer waves which can be obtained by solving the eigen-problem of the homogeneous linearized stability equations. 3. Breakdown to turbulence caused by non-linear secondary instabilities and three-dimensional effects when the unstable waves reach certain amplitude. This three-stage-transition mechanism is path 1 as shown in Fig. 1. With the disturbance amplitude increasing, transient growth, arising through the non-orthogonal nature of the Orr-Sommerfeld eigenfunctions and the Squire eigenfunctions, becomes important. Weak transient growth provides higher initial amplitude for modal growth (path 2) whereas strong transient growth can lead to secondary instabilities and breakdown to turbulence right after the receptivity process (path 3). In the current study, only small amplitude disturbances are considered. Regular porous coating is used to stabilize the boundary layer by attenuating modal growth.

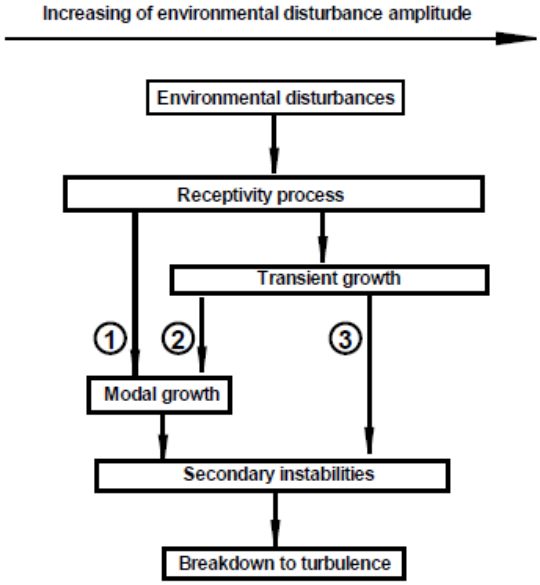

Fig. 1. Paths of external shear flow transition with respect to the amplitude of environmenta disturbance[3].

For the stability of hypersonic boundary layers, different terminologies on boundary-layer wave modes have been used in the literatures [4]. Mathematically, the terminologies of mode S and mode F are more clear and recommended for both mathematical analyses and the interpretation of numerical simulation results [4]. Mode S and mode F are given the names because they are tuned to slow and fast acoustic waves, respectively, in the limit of small Reynolds numbers. Mode F is generally stable whereas mode S is unstable in the region bounded by the neutral curve. Mode S constitutes Mack's first mode, second mode, etc. [5]. The first mode may be inviscidly unstable at sufficiently high Mach numbers because compressible boundary-layer profiles contain an inflection point, but its instability is most important at finite Reynolds number. For boundary layers over adiabatic wall, the second mode exists when flow Mach numbers are above 2.2 and becomes important when Mach numbers are larger than 4. Mack's second mode is physically an acoustic wave. The mechanism of porous coating's absorbing energy from Mack's second mode is similar to that of car exhaust muffler's reducing the amount of noise emitted by the exhaust of an internal combustion engine.

In the past decade, passive control of boundary-layer transition by using porous coating has been studied by theoretical analyses [6-8], experiments [9-14], and numerical simulations [15-19]. Fedorov et al. [6] theoretically analyzed the second-mode instability of a hypersonic boundary layer over a flat plate covered by an ultrasonically absorptive coating (UAC). They found that the second-mode growth was massively reduced, because the porous coating absorbed some energy from the disturbance. Chokani et al. [7] studied the nonlinear aspects of the second-mode stabilization of regular porous coating using bispectral analysis. The spectral measurements showed that the harmonic resonance of the second mode is completely absent on the porous surface, and the first mode is moderately destabilized. Fedorov and Malmuth [8] conducted parametric studies on the performance of regular porous coating for Mach 7 and 10 freestream conditions. They found that the performance strongly increases with porosity.

Rasheed et al. [9] experimentally studied the stability of a Mach 5 boundary layer on a sharp 5.06-degree half-angle cone at zero angle of attack. The cone had a smooth surface around half the cone circumference and an UAC surface on the other half. Their experiments indicated that, when the pore size was significantly smaller than the disturbance wavelength, the porous surface was highly effective in stabilizing the second mode and delaying transition. The experiments carried out by Fedorov and his colleagues [10-12] also showed that porous coating strongly stabilized the second mode and marginally destabilized the first mode. Maslov [13] experimentally studied the stabilization of a hypersonic boundary layer by porous coatings. In his experiments, both regular structure UAC and random felt-metal UAC are used. The results confirmed that porous coatings strongly stabilize the second mode and marginally destabilize the first mode. Compared with regular UAC, felt-metal UAC is much stronger in first-mode destabilization. Lukashevich et al. [14] studied the effect of porous coating thickness on the stabilization of a high-speed boundary layer. They demonstrated that the stabilization effect essentially depends on the UAC thickness and figured out the optimal thickness.

Egorov et al. [16] studied the effect of porous coating on the stability and receptivity of a Mach 6 flat-plate boundary layer by two-dimensional numerical simulation. They found that a regular porous coating effectively diminishes the second-mode growth rate, while weakly affecting acoustic waves. Sandham and Lüdeke [17] numerically studied Mack mode instability of a Mach 6 boundary layer over a porous surface. It was showed that the detailed surface structure is not as important as the overall porosity. Wang and Zhong [18] studied the stabilization of a Mach 5.92 flat-plate boundary layer by using local sections of felt-metal porous coating. Artificial disturbances corresponding to a single boundary-layer wave were introduced near the leading edge. It was found that disturbances are destabilized or stabilized when porous coating is located upstream or downstream of the synchronization point. For felt-metal porous coating, the destabilization of Mack's first mode is significant.

However, there is only quite limited studies on the stabilization efficiency of porous coating. And no work has been reported about the thermochemical non-equilibrium effects of hypersonic flows on the stabilization efficiency of porous coating. In this paper, the stabilization of a Mach 5.92 flat-plate boundary layer by using regular coating is first studied for perfect gas flow. Since numerical simulations based on perfect gas flow may not be enough. The effects of thermochemical non-equilibrium flow including internal energy excitations, translation-vibration energy relaxation, and chemical reactions among different species need to be considered. We have developed a new high-order shock-fitting solver for non-equilibrium flow simulations based on the 5-species air chemistry and recently thermal non-equilibrium models. The code package has been tested and is being applied to numerical simulation of a Mach 12.56 boundary layer over a blunted wedge of a half angle 20 degree.

2. Governing equations and numerical methods

2.1 Governing equations of perfect gas flow

The governing equations of perfect gas flow are written in the following conservation-law form in the Cartesian coordinates,

$$\frac{\partial U}{\partial t}+\frac{\partial F_j}{\partial x_j}+\frac{\partial F_{vj}}{\partial x_j}=0 \tag{1}$$

where U, F_j and F_{vj} are the vectors of conservative variables, convective and viscous flux in the direction of jth coordinate, respectively, i.e.,

$$U=\{\rho,\rho u_1,\rho u_2,\rho u_3,e\} \tag{2}$$

$$F_j=\begin{Bmatrix}\rho u_j\\ \rho u_1u_j+P\delta_{1j}\\ \rho u_2u_j+P\delta_{1j}\\ \rho u_3u_j+P\delta_{1j}\\ (e+p)u_j\end{Bmatrix},\ F_{vj}=\begin{Bmatrix}0\\ -\tau_{1j}\\ -\tau_{2j}\\ -\tau_{3j}\\ -\tau_{jk}u_k+q_j\end{Bmatrix} \tag{3}$$

For the simulation of perfect gas flow, the following equations are needed.

$$P=\rho RT \tag{4}$$

$$e=\rho(c_vT+\frac{1}{2}u_ku_k) \tag{5}$$

$$\tau_{ij}=\mu(\frac{\partial u_i}{\partial x_j}+\frac{\partial u_j}{\partial x_i})+\delta_{ij}\lambda\frac{\partial u_k}{\partial x_k} \tag{6}$$

$$q_j=-k\frac{\partial T}{\partial x_j} \tag{7}$$

where R is the gas constant. The specific heat c_v is a constant determined by a given ratio of specific heats γ. The viscosity coefficient μ is calculated by Sutherland's law,

$$\mu=\mu_r\left(\frac{T}{T_0}\right)^{3/2}\frac{T_0+T_s}{T+T_s} \tag{8}$$

For air, $\mu_r=1.7894\times10^{-5}$ Ns/m^2, $T_0=288.0$ K, $T_s=110.33$ K, and $\lambda=-2\mu/3$. The heat conductivity coefficient k is computed by a given Prandtl number.

2.2 Governing equations of thermochemical non-equilibrium flow

The governing equations of thermochemical non-equilibrium flow based on 5-species air chemistry are Navier-Stokes equations with source terms (no radiation). Specifically, they consist of the flowing equations,

$$\frac{\partial\rho_s}{\partial t}+\frac{\partial}{\partial x_j}(\rho_su_j)-\frac{\partial}{\partial x_j}(\rho D_s\frac{\partial y_s}{\partial x_j})=\omega_s \tag{9}$$

$$\frac{\partial}{\partial t}(\rho u_i)+\frac{\partial}{\partial x_j}(\rho u_i u_j+p\delta_{ij})-\frac{\partial}{\partial x_j}\left[\mu\left(\frac{\partial u_i}{\partial x_j}+\frac{\partial u_j}{\partial x_i}\right)-\frac{2}{3}\mu\frac{\partial u_k}{\partial x_k}\delta_{ij}\right]=0 \tag{10}$$

$$\frac{\partial \rho E}{\partial t}+\frac{\partial}{\partial x_j}(\rho H u_j)-\frac{\partial}{\partial x_j}\left[u_i\mu\left(\frac{\partial u_i}{\partial x_j}+\frac{\partial u_j}{\partial x_i}\right)-\frac{2}{3}u_i\mu\frac{\partial u_k}{\partial x_k}\delta_{ij}\right]$$
$$-\frac{\partial}{\partial x_j}\left(\rho\sum_{s=1}^{5}h_s D_s\frac{\partial y_s}{\partial x_j}\right)-\frac{\partial}{\partial x_j}\left(K\frac{\partial T}{\partial x_j}+K_V\frac{\partial T_V}{\partial x_j}\right)=0 \tag{11}$$

$$\frac{\partial \rho E_V}{\partial t}+\frac{\partial}{\partial x_j}(\rho E_V u_j)-\frac{\partial}{\partial x_j}(\rho\sum_{s=1}^{5}e_{V,s}D_s\frac{\partial y_s}{\partial x_j})-\frac{\partial}{\partial x_j}\left(K_V\frac{\partial T_V}{\partial x_j}\right)=\sum_{s=1}^{3}Q_{T-V,s}+\sum_{s=1}^{5}\omega_s e_{V,s} \tag{12}$$

where,

$$\rho=\sum_{s=1}^{5}\rho_s \qquad u_j=\frac{1}{\rho}\sum_{s=1}^{5}\rho_s u_{sj} \qquad y_s=\frac{(\rho_s/M_s)}{\sum_{i=1}^{5}(\rho_i/M_i)}$$

$$p=\sum_{s=1}^{5}p_s=\sum_{s=1}^{5}\frac{\rho_s\bar{R}T}{M_s} \qquad E=\frac{u_i u_i}{2}+\sum_{s=1}^{5}\frac{\rho_s e_s}{\rho} \qquad H=E+\frac{p}{\rho}$$

$\bar{R}$ is the universal gas constant. The formulas of species diffusion coefficient D_s, viscosity μ, heat conductivities K and K_V, species internal energy e_s and $e_{V,s}$, specific vibration energy E_V, and source terms depends on the models of thermochemical non-equilibrium flow.

The corresponding matrix form of governing equations is as follows,

$$\frac{\partial U}{\partial t}+\frac{\partial F_j}{\partial x_j}+\frac{\partial G_j}{\partial x_j}=S \tag{13}$$

where the vector of conservative variables has ten components,

$$U=\left(\rho_1,\rho_2,\ldots,\rho_5,\rho u,\rho v,\rho w,\rho E,\rho e_V\right)^{\mathrm{T}} \tag{14}$$

The inviscid and viscous flux in the direction of jth coordinate, F_j and G_j, and the source term S are given below.

$$F_j=\begin{pmatrix}\rho_1 u_j\\ \rho_2 u_j\\ \vdots\\ \rho_5 u_j\\ \rho u u_j+p\delta_{1j}\\ \rho v u_j+p\delta_{2j}\\ \rho w u_j+p\delta_{3j}\\ \rho H u_j\\ \rho e_V u_j\end{pmatrix},\ G_j=\begin{pmatrix}\rho_1 v_{1j}\\ \rho_2 v_{2j}\\ \vdots\\ \rho_5 v_{5j}\\ -\tau_{1j}\\ -\tau_{2j}\\ -\tau_{3j}\\ -u_i\tau_{ij}+q_j+q_{Vj}+\sum_{s=1}^{5}\rho_s h_s v_{sj}\\ q_{Vj}+\sum_{s=1}^{5}\rho_s e_{V,s}v_{sj}\end{pmatrix},\ S=\begin{pmatrix}\omega_1\\ \omega_2\\ \vdots\\ \omega_5\\ 0\\ 0\\ 0\\ 0\\ \sum_{s=1}^{3}(Q_{T-V,s}+\omega_s e_{V,s})\end{pmatrix} \tag{15}$$

In above equations, $v_{sj} = u_{sj} - u_j$ is diffusion velocity of species s.

$$v_{sj} = -\frac{\rho D_s}{\rho_s}\frac{\partial y_s}{\partial x_j} \tag{16}$$

The model of vibration and electron energy used in Hash et al.'s paper [20] are implemented in the code. Specific total enthalpy of species and specific heat in constant pressure of species are defined as,

$$h_s = c_{vs}T + \frac{p_s}{\rho_s} + e_{V,s} + h_s^0 \tag{17}$$

$$c_p^s = c_v^s + \frac{\overline{R}}{M_s} + c_V^s \tag{18}$$

where h_s^0 is the generation enthalpy of species. The variables on the right hand side of equations (17) and (18) are calculated from the following formula,

$$e_{V,s} = (e_V + e_{els}) = \frac{\overline{R}}{M_s}\left(\sum_{s=1}^{3}\frac{\theta_{vs}}{e^{\theta_{vs}/T_V}-1} + \sum_{s=1}^{5}\frac{\sum_{i=1}^{\infty} g_{i,s}\theta_{el,i,s}\exp(-\theta_{el,i,s}/T_V)}{\sum_{i=0}^{\infty} g_{i,s}\exp(-\theta_{el,i,s}/T_V)}\right) \tag{19}$$

$$c_v^s = c_{vtr,s} + c_{vrot,s} \tag{20}$$

$$c_{vtr,s} = \frac{3\overline{R}}{2M_s} \tag{21}$$

$$c_{vrot,s} = \begin{cases} \dfrac{\overline{R}}{M_s} & (s = 1,3) \\ 0 & (otherwise) \end{cases} \tag{22}$$

$$c_V^s = \frac{\overline{R}}{M_s}\left\{\frac{\left(\theta_{vs}/T_V\right)^2 e^{\theta_{vs}/T_V}}{\left(e^{\theta_{vs}/T_V}-1\right)^2} + \frac{\left[\sum_{i=1}^{\infty} g_{i,s}\left(\theta_{el,i,s}/T_V\right)^2\exp(-\theta_{el,i,s}/T_V)\right]}{\sum_{i=0}^{\infty} g_{i,s}\exp(-\theta_{el,i,s}/T_V)}\right.$$
$$\left. - \frac{\left[\sum_{i=1}^{\infty} g_{i,s}\theta_{el,i,s}\exp(-\theta_{el,i,s}/T_V)\right]\left[\sum_{i=0}^{\infty} g_{i,s}\left(\theta_{el,i,s}/T_V^2\right)\exp(-\theta_{el,i,s}/T_V)\right]}{\left(\sum_{i=0}^{\infty} g_{i,s}\exp(-\theta_{el,i,s}/T_V)\right)^2}\right\} \tag{23}$$

For the 5-species air, the related parameters used in the models of vibration and electron energy are listed in Table 1 and Table 2. Compared to other models [21, 22], the current models have the advantage of directly applicable to unlimited high temperatures.

Table 1. Parameters used vibration energy model

Species	h_s^0 (J/kg)	M_s (g)	θ_{vs} (K)
N2	0	28	3395
O2	0	32	2239
NO	2.996123e6	30	2817
N	3.362161e7	14	-
O	1.543119e7	16	-

Table 2. Electronic energy states for 5-species air

Species	Θ (K)	g	Species	Θ (K)	g	Species	ΘO (K)	g
N2	0	1	O2	1.13916e4	2	NO	8.88608e4	4
N2	7.22316e4	3	O2	1.89847e4	1	NO	8.98176e4	4
N2	8.57786e4	6	O2	4.75597e4	1	NO	8.98845e4	2
N2	8.60503e4	6	O2	4.99124e4	6	NO	9.04270e4	2
N2	9.53512e4	3	O2	5.09227e4	3	NO	9.06428e4	2
N2	9.80564e4	1	O2	7.18986e4	3	NO	9.11176e4	4
N2	9.96827e4	2	NO	0	4	N	0	4
N2	1.04898e5	2	NO	5.46735e4	8	N	2.76647e4	10
N2	1.11649e5	5	NO	6.31714e4	2	N	4.14931e4	6
N2	1.22584e5	1	NO	6.59945e4	4	O	0	5
N2	1.24886e5	6	NO	6.90612e4	4	O	2.27708e2	3
N2	1.28248e5	6	NO	7.0500e4	4	O	3.26569e2	1
N2	1.33806e5	10	NO	7.49106e4	4	O	2.28303e4	5
N2	1.40430e5	6	NO	7.62888e4	2	O	4.86199e4	1
N2	1.50496e5	6	NO	8.67619e4	4			
O2	0	3	NO	8.71443e4	2			

For the 5-species air, a more complex model of thermal properties is applied [23]. Thermal properties are calculated as follows,

$$\mu = \sum_s \frac{m_s \gamma_s}{\sum_r \gamma_r \Delta_{sr}^{(2)}(T)} \quad \textbf{(g/cm-sec)} \tag{24}$$

$$K_T = \frac{15}{4} k \sum_s \frac{\gamma_s}{\sum_r a_{sr} \gamma_r \Delta_{sr}^{(2)}(T)} \quad \textbf{(J/cm-sec-K)} \tag{25}$$

In above equation, $a_{sr} = 1 + \frac{\left[1-(m_s/m_r)\right]\left[0.45-2.54(m_s/m_r)\right]}{\left[1+(m_s/m_r)\right]^2}$.

$$K_R = k \sum_{s=1,2,3} \frac{\gamma_s}{\sum_r \gamma_r \Delta_{sr}^{(1)}(T)} \quad \textbf{(J/cm-sec-K)} \tag{26}$$

$$K_{V-E} = k \frac{C_{V,V}}{R} \sum_{s=1}^{5} \frac{\gamma_s}{\sum_r \gamma_r \Delta_{sr}^{(1)}(T)} \quad \textbf{(J/cm-sec-K)} \tag{27}$$

To calculate viscosity and heat conductivity, the collision terms are as follows,

$$\Delta_{sr}^{(1)}(T)=\frac{8}{3}\left[\frac{2m_s m_r}{\pi RT(m_s+m_r)}\right]^{1/2}10^{-20}\pi\Omega_{sr}^{(1,1)}(T)\ \textbf{(cm-sec)}$$

$$\Delta_{sr}^{(2)}(T)=\frac{16}{3}\left[\frac{2m_s m_r}{\pi RT(m_s+m_r)}\right]^{1/2}10^{-20}\pi\Omega_{sr}^{(2,2)}(T)\ \textbf{(cm-sec)}$$

Collision integrals involving neutrals (Non-Coulombic collision integrals) are

$$\pi\Omega_{sr}^{(l,j)}(T)=DT^{\left[A(\ln T)^2+B\ln T+C\right]}\ (\overset{0}{\mathrm{A}}^2) \tag{28}$$

Species diffusion coefficients are defined as,

$$D_s=\frac{(1-y_s)}{\sum_{r\neq s}(y_r/D_{sr})} \tag{29}$$

For binary diffusion between heavy particles, $D_{sr}=\dfrac{kT}{p\Delta_{sr}^{(1)}(T)}$. The heat conductivities K and K_V in governing equations are calculated as,

$$K=K_T+K_R \tag{30}$$

$$K_V=K_{V-E} \tag{31}$$

For chemical non-equilibrium, five reactions are considered for the five species air, i.e.,

$$\left.\begin{aligned} N_2+M&=2N+M\\ O_2+M&=2O+M\\ NO+M&=N+O+M\\ N_2+O&=NO+N\\ NO+O&=O_2+N \end{aligned}\right\} \tag{32}$$

Correspondingly, the reaction rates are calculated as follows,

$$\left\{\begin{aligned} R_1&=\sum_m\left[-k_{f_1m}\frac{\rho_{N_2}}{M_{N_2}}\frac{\rho_m}{M_m}+k_{b_1m}\frac{\rho_N}{M_N}\frac{\rho_N}{M_N}\frac{\rho_m}{M_m}\right]\\ R_2&=\sum_m\left[-k_{f_2m}\frac{\rho_{O_2}}{M_{O_2}}\frac{\rho_m}{M_m}+k_{b_2m}\frac{\rho_O}{M_O}\frac{\rho_O}{M_O}\frac{\rho_m}{M_m}\right]\\ R_3&=\sum_m\left[-k_{f_3m}\frac{\rho_{NO}}{M_{NO}}\frac{\rho_m}{M_m}+k_{b_3m}\frac{\rho_N}{M_N}\frac{\rho_O}{M_O}\frac{\rho_m}{M_m}\right]\\ R_4&=-k_{f_4}\frac{\rho_{N_2}}{M_{N_2}}\frac{\rho_O}{M_O}+k_{b_4}\frac{\rho_{NO}}{M_{NO}}\frac{\rho_N}{M_N}\\ R_5&=-k_{f_5}\frac{\rho_{NO}}{M_{NO}}\frac{\rho_O}{M_O}+k_{b_5}\frac{\rho_{O_2}}{M_{O_2}}\frac{\rho_N}{M_N} \end{aligned}\right. \tag{33}$$

Finally, the source terms are as follows,

$$\begin{cases} \omega_{N_2} = M_{N_2}(R_1 + R_4) \\ \omega_{O_2} = M_{O_2}(R_2 - R_5) \\ \omega_{NO} = M_{NO}(R_3 - R_4 + R_5) \\ \omega_N = M_N(-2R_1 - R_3 - R_4 - R_5) \\ \omega_O = M_O(-2R_2 - R_3 + R_4 + R_5) \end{cases} \tag{34}$$

The forward and backward reaction rate coefficients have the form of

$$k_f\left(\overline{T}\right) = C_f \overline{T}^{\eta_f} \exp\left(-\theta_f / \overline{T}\right) \tag{35}$$

$$k_b\left(T\right) = \frac{k_f(T)}{k_{eq}(T)} \tag{36}$$

For dissociation reactions, $\overline{T} = \sqrt{TT_V}$. For the other reactions, the control temperature is $\overline{T} = T$. The equilibrium constant is obtained using the curve fits of Park [24], i.e.,

$$k_{eq} = \exp(a_1 z^{-1} + a_2 + a_3 \ln z + a_4 z + a_5 z^2) \tag{37}$$

In two temperature model, energy relaxation only happens between translation energy and vibration & electron energy, which can be expressed as

$$Q_{T-v,s} = \rho_s \frac{e_{vs}^*(T) - e_{vs}}{\tau_{vs}} \tag{38}$$

where, $e_{vs}^*(T)$ is the vibration energy per unit mass of species s evaluated at the local translational temperature.

$$\tau_{vs} = \left\langle \tau_{s,L-T} \right\rangle + \tau_{cs} = \frac{\sum_r y_r}{\sum_r y_r / \tau_{sr,L-T}} + \frac{1}{a_s \sigma_v N_s} \qquad (a_s = \sqrt{\frac{8\overline{R}T}{\pi M_s}})$$

$$\tau_{sr,L-T} = \frac{1}{p} \exp\left[A_{sr}\left(T^{-1/3} - 0.015\mu_{sr}^{1/4}\right) - 18.42 \right] \text{ (p in atm)}$$

$$A_r = 1.16 \times 10^{-3} \mu_{sr}^{1/2} \theta_{vs}^{4/3} \qquad \mu_{sr} = M_s M_r / (M_s + M_r)$$

$$S_s = 3.5 \exp\left(-\theta_s / T_{shk}\right) \qquad \sigma_v = 10^{-21}\left(50,000 / T\right)^2$$

Here, θ_s is a defined characteristic temperature listed in Table 1.

2.3 Coordinate transform

The flow solver uses structured grids. The following grid transform is applied in the computational domain,

$$\begin{cases} x = x(\xi, \eta, \zeta, \tau) \\ y = y(\xi, \eta, \zeta, \tau) \\ z = z(\xi, \eta, \zeta, \tau) \\ t = \tau \end{cases} \Leftrightarrow \begin{cases} \xi = \xi(x, y, z, t) \\ \eta = \eta(x, y, z, t) \\ \zeta = \zeta(x, y, z, t) \\ \tau = t \end{cases} \tag{39}$$

The Jacobian of the above coordinate transform is,

$$J=\begin{vmatrix} x_\xi & y_\xi & z_\xi & 0 \\ x_\eta & y_\eta & z_\eta & 0 \\ x_\zeta & y_\zeta & z_\zeta & 0 \\ x_\tau & y_\tau & z_\tau & 1 \end{vmatrix} \tag{40}$$

With the transform, the governing equations in (ξ,η,ζ,τ) coordinate system are written as

$$\frac{\partial(JU)}{\partial\tau}+\frac{\partial\tilde{F}_1}{\partial\xi}+\frac{\partial\tilde{F}_2}{\partial\eta}+\frac{\partial\tilde{F}_3}{\partial\zeta}+\frac{\partial\tilde{G}_1}{\partial\xi}+\frac{\partial\tilde{G}_2}{\partial\eta}+\frac{\partial\tilde{G}_3}{\partial\zeta}=JS \tag{41}$$

where

$$\begin{aligned}
\tilde{F}_1 &= J\xi_x F_1 + J\xi_y F_2 + J\xi_z F_3 + JU\xi_t \\
\tilde{F}_2 &= J\eta_x F_1 + J\eta_y F_2 + J\eta_z F_3 + JU\eta_t \\
\tilde{F}_3 &= J\zeta_x F_1 + J\zeta_y F_2 + J\zeta_z F_3 + JU\zeta_t \\
\tilde{G}_1 &= J\xi_x G_1 + J\xi_y G_2 + J\xi_z G_3 \\
\tilde{G}_2 &= J\eta_x G_1 + J\eta_y G_2 + J\eta_z G_3 \\
\tilde{G}_3 &= J\zeta_x G_1 + J\zeta_y G_2 + J\zeta_z G_3
\end{aligned}$$

2.4 Numerical method

The governing equations are solved by the fifth-order shock-fitting method of Zhong [25]. For the thermochemical non-equilibrium system (13) in the direction, $\mathrm{k}=(k_1,k_2,k_3)$, the corresponding inviscid flux term is

$$\mathrm{F}=\begin{pmatrix} \rho_1\,\mathrm{k\,u} \\ \rho_2\,\mathrm{k\,u} \\ \rho_3\,\mathrm{k\,u} \\ \rho_4\,\mathrm{k\,u} \\ \rho_5\,\mathrm{k\,u} \\ \rho u\,\mathrm{k\,u}+pk_1 \\ \rho v\,\mathrm{k\,u}+pk_2 \\ \rho w\,\mathrm{k\,u}+pk_3 \\ \rho H\,\mathrm{k\,u} \\ \rho E_V\,\mathrm{k\,u} \end{pmatrix} \tag{42}$$

Hence the Jacobian of flux is defined as,

$$\mathrm{A}=\frac{\partial\mathrm{F}}{\partial\mathrm{U}}=L\Lambda R \tag{43}$$

$$A=|\mathrm{k}|\begin{bmatrix}\tilde{U}(\delta_{sr}-c_s) & c_s n_x & c_s n_y & c_s n_z & 0 & 0\\ \tilde{\gamma}_r n_x-\tilde{U}u & -\beta u n_x+u n_x+\tilde{U} & -\beta v n_x+u n_y & -\beta w n_x+u n_z & \beta n_x & \phi n_x\\ \tilde{\gamma}_r n_y-\tilde{U}v & -\beta u n_y+v n_x & -\beta v n_y+v n_y+\tilde{U} & -\beta w n_y+v n_z & \beta n_y & \phi n_y\\ \tilde{\gamma}_r n_z-\tilde{U}w & -\beta u n_z+w n_x & -\beta v n_z+w n_y & -\beta w n_z+w n_z+\tilde{U} & \beta n_z & \phi n_z\\ \tilde{\gamma}_r\tilde{U}-\tilde{U}H & -\beta u\tilde{U}+H n_x & -\beta v\tilde{U}+H n_y & -\beta w\tilde{U}+H n_z & \beta\tilde{U}+\tilde{U} & \phi\tilde{U}\\ -\tilde{U}e_V & e_V n_x & e_V n_y & e_V n_z & 0 & \tilde{U}\end{bmatrix}$$

$$R=\begin{bmatrix}a^2\delta_{sr}-c_s\tilde{\gamma}_r & \beta u c_s & \beta v c_s & \beta w c_s & -\beta c_s & -\phi c_s\\ -\tilde{V} & l_x & l_y & l_z & 0 & 0\\ -\tilde{W} & m_x & m_y & m_z & 0 & 0\\ \tilde{\gamma}_r-\tilde{U}a & a n_x-\beta u & a n_y-\beta v & a n_z-\beta w & \beta & \phi\\ \tilde{\gamma}_r+\tilde{U}a & -a n_x-\beta u & -a n_y-\beta v & -a n_z-\beta w & \beta & \phi\\ -e_V\tilde{\gamma}_r & \beta u e_V & \beta v e_V & \beta w e_V & -\beta e_V & a^2-\phi e_V\end{bmatrix}$$

$$L=\begin{bmatrix}\delta_{sr}/a^2 & 0 & 0 & c_s/2a^2 & c_s/2a^2 & 0\\ u/a^2 & l_x & m_x & (u+a n_x)/2a^2 & (u-a n_x)/2a^2 & 0\\ v/a^2 & l_y & m_y & (v+a n_y)/2a^2 & (v-a n_y)/2a^2 & 0\\ w/a^2 & l_z & m_z & (w+a n_z)/2a^2 & (w-a n_z)/2a^2 & 0\\ \left[\beta(u^2+v^2+w^2)-\tilde{\gamma}_r\right]/\beta a^2 & \tilde{V} & \tilde{W} & (H+a\tilde{U})/2a^2 & (H-a\tilde{U})/2a^2 & -\phi/\beta a^2\\ 0 & 0 & 0 & e_V/2a^2 & e_V/2a^2 & 1/a^2\end{bmatrix}$$

The eigenvalues of Jacobian matrix (43) are

$$\lambda_{1,2,5}=|\mathrm{k}|\tilde{U} \tag{44}$$

$$\lambda_3=|\mathrm{k}|(\tilde{U}+a) \tag{45}$$

$$\lambda_4=|\mathrm{k}|(\tilde{U}-a) \tag{46}$$

where subscript "s" refers to row s and species s, whereas subscript "r" refers to column r and species r. Both s and r vary from 1 to 5 in the present model. The unit vector n is defined from vector k as

$$\mathrm{n}=(n_x,n_y,n_z)=\frac{(k_1,k_2,k_3)}{|\mathrm{k}|} \tag{47}$$

$\mathrm{l}=\left(l_x,l_y,l_z\right)$ and $\mathrm{m}=\left(m_x,m_y,m_z\right)$ are two unit vectors such that n, l, and m are mutually orthogonal. Furthermore, we have,

$$\tilde{U}=un_x+vn_y+wn_z \tag{48}$$

$$\tilde{V}=ul_x+vl_y+wl_z \tag{49}$$

$$\tilde{W}=um_x+vm_y+wm_z \tag{50}$$

The derivative of pressure respecting to conservative variables comes from

$$dp = \beta(d\rho E - ud\rho u - vd\rho v - wd\rho w) + \phi d\rho e_V + \tilde{\gamma}_s d\rho_s \tag{51}$$

where

$$\beta = \frac{\bar{R}}{\rho \sum_s c_s c_{v,tr}^s} \sum_{r=1}^{5} \frac{\rho_r}{M_r} \tag{52}$$

$$\phi = \frac{\bar{R}}{\rho C_{v,V}} \frac{\rho_e}{M_e} - \beta \tag{53}$$

$$\tilde{\gamma}_s = \frac{\bar{R} T_q}{M_s} + \beta \frac{u^2 + v^2 + w^2}{2} - \beta e_s - \phi e_{V,s} \tag{54}$$

$$a^2 = \sum_{s=1}^{5} c_s \tilde{\gamma}_s + \beta \left[H - (u^2 + v^2 + w^2) \right] + \phi e_V = (1 + \beta) \frac{p}{\rho} \tag{55}$$

In equation (54), $T_q = T_V$ when s is an electron, otherwise, $T_q = T$.

In shock-fitting method, the velocity and location of the shock are solved as part of the solutions. The flow variables behind the shock are determined by Rankine-Hugoniot relations across the main shock and a characteristic compatibility relation from behind the shock. With the assumptions of "frozen" flow (no chemical reactions and energy relaxations when flow passes through the shock), the species mass fractions and vibration temperature keep constant on the two sides of the shock where translation temperature jumps across the shock. In this way, shock jumps conditions for total density, momentum and total energy are the same as those for perfect gas. In addition, the compatibility relation relating to the maximum eigenvalue in wall normal direction is used.

In the interior, compressible Navier-Stokes equations are solved in fully conservative form. An explicit finite difference scheme is used for spatial discretization of the governing equation, the inviscid flux terms are discretized by a fifth-order upwind scheme, and the viscous flux terms are discretized by a sixth-order central scheme. For the inviscid flux vectors, the flux Jacobians contain both positive and negative eigenvalues. A simple local Lax-Friedrichs scheme is used to split vectors into negative and positive wave fields. For example, the flux term F in Eq. (42) can be split into two terms of pure positive and negative eigenvalues as follows

$$F = F_+ + F_- \tag{56}$$

where $F_+ = \frac{1}{2}(F + \lambda U)$ and $F_- = \frac{1}{2}(F - \lambda U)$ and λ is chosen to be larger than the local maximum eigenvalue of F′.

$$\lambda = \frac{|\nabla \eta|}{J} \left(\sqrt{(\varepsilon c)^2 + u'^2} + c \right) \tag{57}$$

where

$$u' = \frac{\eta_x u + \eta_y v + \eta_z w + \eta_t}{|\nabla \eta|} \tag{58}$$

The parameter ε is a small positive constant added to adjust the smoothness of the splitting. The fluxes F_+ and F_- contain only positive and negative eigenvalues respectively. Therefore, in the spatial discretization, the derivative of the flux F is split into two terms

$$\frac{\partial F}{\partial \eta} = \frac{\partial F_+}{\partial \eta} + \frac{\partial F_-}{\partial \eta} \tag{59}$$

where the first term on the right hand side is discretized by the upwind scheme and the second term by the downwind scheme.

The fifth-order explicit scheme utilizes a 7-point stencil and has an adjustable parameter α as follows

$$u_i' = \frac{1}{hb_i}\sum_{k=-3}^{3} a_{i+k}u_{i+k} - \frac{\alpha}{6!b_i}h^5\left(\frac{\partial^6 u}{\partial x^6}\right)_i + \ldots \tag{60}$$

where $\alpha_{i\pm3} = \pm 1 + \frac{1}{12}\alpha,\ \alpha_{i\pm2} = \mp 9 - \frac{1}{2}\alpha,\ \alpha_{i\pm1} = \pm 45 + \frac{5}{4}\alpha,\ \alpha_i = -\frac{5}{3}\alpha$ and $b_i = 60$. The scheme is upwind when α < 0 and downwind when α > 0. It becomes a 6-order central scheme when α = 0 which is used for discretizing viscous terms. However, for shock and turbulence interaction problems, sufficiently high turbulence intensities might produce secondary shocks behind the main shock. To handle such cases, a shock-capturing scheme based on WENO is used. All our methods are coded using FORTRAN77 & 90 while Message Passing Interface (MPI) is used for communication in the parallel computations.

3. Model of regular porous coating

In the passive control of hypersonic boundary-layer transition by using porous coating, feltmetal coating is initially used [6, 10], because its structure is quite similar to that of the material currently used in thermal protection system. Later, regular coating has been used in most of the researches in this area due to its convenience for parametric studies and new coating design [16, 17]. In the current simulation, regular coatings are modeled by pressure perturbation related wall blowing-suction. The wall blowing-suction induced by porous coating is as follows,

$$v' = A_y p' \tag{61}$$

The porous coating admittance, A_y, is defined as,

$$A_y = -\frac{\phi}{Z_0}\tanh(\Lambda h) \tag{62}$$

In above equation, ϕ is porosity, h is the porous-layer thickness non-dimensionalized by the local length scale of boundary-layer thickness,

$$h = \frac{h^*}{L^*} = h^*\sqrt{\frac{\rho_\infty^* u_\infty^*}{\mu_\infty^* x^*}} \tag{63}$$

According to Allard and Champoux's theoretical analyses [26], the empirical equations for porous coating characteristic impedance (Z_0) and propagation constant (Λ) depend on wall temperature, wall density, and edge Mach number of the boundary layer,

$$Z_0 = \frac{\rho_w}{M_e}\sqrt{T_w}\sqrt{\tilde{\rho}/\tilde{C}} \tag{64}$$

$$\Lambda = \frac{i\omega M_e}{\sqrt{T_w}}\sqrt{\tilde{\rho}\tilde{C}} \tag{65}$$

where ρ_w and T_w are the local dimensionless density and temperature on porous surface. The edge Mach number (M_e) is defined right after the shock.

For regular porous coating considered in the current paper, the dynamic density ($\tilde{\rho}$) and the bulk module ($\tilde{C}$) are calculated from the following equations,

$$\tilde{\rho} = -\frac{J_0(k_v)}{J_2(k_v)} \tag{66}$$

$$\tilde{C} = \gamma + (\gamma - 1)\frac{J_2(k_t)}{J_0(k_t)} \tag{67}$$

In above two equations, k_v and k_t are defined as

$$k_v = \sqrt{-\frac{i\omega^* \rho_w^* r^{*2}}{\mu_w^*}} \tag{68}$$

$$k_t = k_v\sqrt{\mathrm{Pr}} \tag{69}$$

With the definitions of characteristic impedance and propagation constant, regular coating admittance is generally a complex number. Velocity perturbation calculated by Eq. (61) is also a complex number. However, only the real part of velocity perturbation can be imposed in numerical simulations. The unsteady velocity perturbation in numerical simulation is written relating to the instantaneous pressure perturbation ($p(t^*)$).

$$v(t) = \left|A_y\right|\cos(\varphi)\,p(t) + \left|A_y\right|\sin(\varphi)\frac{dp(t)}{\omega dt} \tag{70}$$

4. Stabilization of a Mach 5.92 flat-plate boundary layer

In this paper, the stabilization of a Mach 5.92 flat-plate boundary layer is first studied for perfect gas flow. The flow conditions are listed below.

$M_\infty = 5.92$ $\qquad$ $T_\infty = 48.69\,\mathrm{K}$

$p_\infty = 742.76\,\mathrm{Pa}$ $\qquad$ $\mathrm{Pr} = 0.72$

$\mathrm{Re}_\infty = 14.12\times10^6/\mathrm{m}$

In a previous paper, we have studied the stabilization of the same boundary-layer flow by using local sections of felt-metal porous coating [18]. Since the results of the steady base flow and the stability characteristics have been reported in that paper, they are neglected here.

At first, the spatial development mode S over regular coating is studied by numerical simulations. The stability simulations consist of two steps: 1) periodic disturbances corresponding to mode S at the frequency of 100 kHz are superimposed on steady base flow at a cross-section of the boundary layer to show spatial development of the wave, 2) regular porous coating is used downstream of the superimposed wave to investigate its effect on mode S growth. For the boundary layer waves considered in the current paper, the synchronization point and the two neutral points in x coordinate are respectively located at 0.33184 m, 1.69744×10^{-3} 1.69744 m, and 0.84622 m. In order to study the effect of different porous coatings, one case of numerical

simulation is carried out for feltmetal coating. Figure 2 shows a schematic of the Mach 5.92 flat-plate boundary layer over porous coatings.

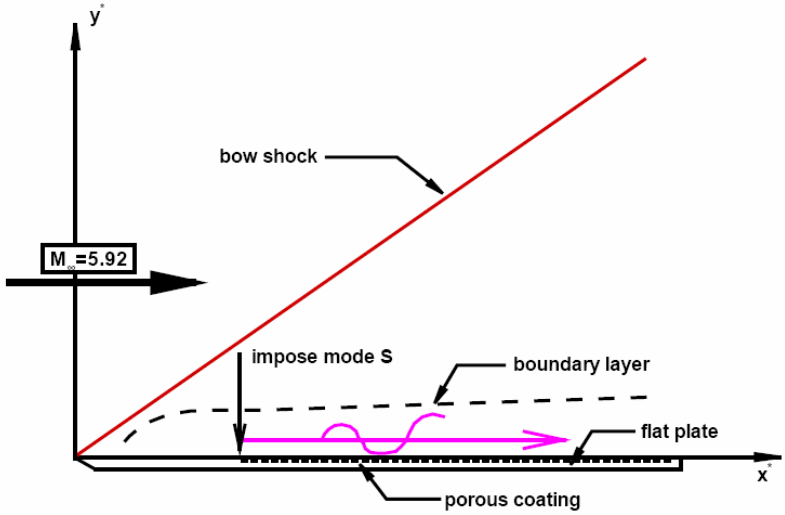

Fig. 2. A schematic of the stabilization of a Mach 5.92 flat-plate boundary layer using porous coating.

Periodic disturbances corresponding to mode S is superimposed on steady base flow at a cross-section of the boundary layer at x = 69.00 mm. The computational domain for stability simulation starts at x = 69.00 mm and ends at x = 0.8590 m. The formula of the disturbances is given below,

$$\begin{Bmatrix} \tilde{u} \\ \tilde{v} \\ \tilde{w} \\ \tilde{p} \\ \tilde{T} \end{Bmatrix} = \varepsilon \begin{Bmatrix} \hat{u}(y) \\ \hat{v}(y) \\ \hat{w}(y) \\ \hat{p}(y) \\ \hat{T}(y) \end{Bmatrix} \sin(\omega t) \tag{71}$$

where the parameters of α_c and β_c are wave number components in streamwise and spanwise directions, and ω_c is the circular frequency. Disturbance vector on the right hand side of Eq. (71) represents the eigenfunction of mode S normalized by the pressure perturbation on the wall. The parameter of disturbance amplitude is assigned to mode S as $\varepsilon = 10^{-8}$, which is small enough to preserve the linear properties of the disturbances.

Figure 3 compares superimposed disturbances of mode S with the eigenfunctions of mode S obtained from LST. In these figures, both superimposed disturbances and the eigenfunctions are normalized by corresponding pressure disturbance on the wall. The good agreements of velocity and pressure profiles indicate that the disturbances superimposed across the boundary layer are exactly mode S. The discrepancy between temperature profiles near the wall (y/L < 10) as shown in Fig. 3(d) is caused by nonparallel flow effect. Temperature profile of superimposed disturbance is calculated using pressure and density eigenfunctions of corresponding wave, and mean flow temperature, pressure, and density. In our simulation, nonparallel flow effect is included in mean flow variables.

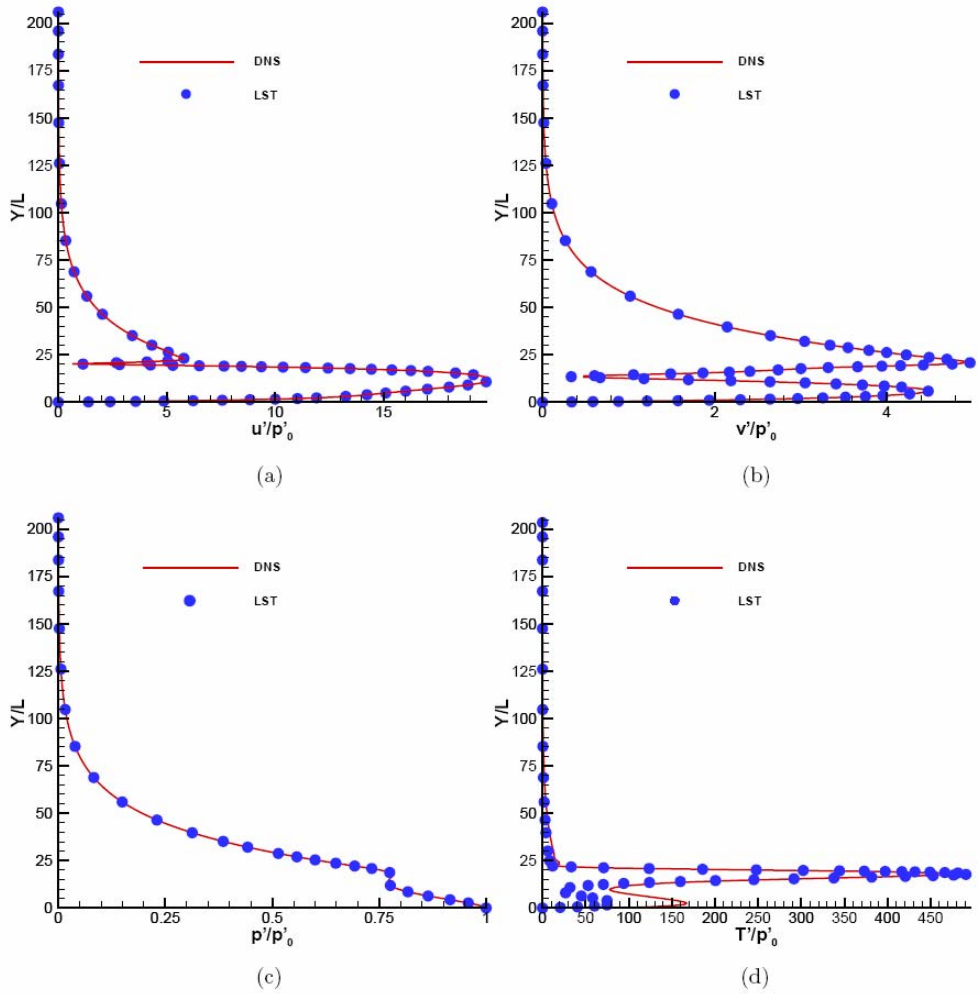

Fig. 3. Comparisons of superimposed disturbance profiles for mode S with the eigenfunction of mode S obtained from LST: (a) streamwise velocity, (b) wall-normal velocity, (c) pressure, (d) temperature.

For regular porous coating, five different porosities are considered. Specifically, the structure parameters are as follows,

$$h^* = 0.45\,\text{mm} \qquad r^* = 25\mu\,\text{m}$$

$$\phi_1 = \pi/4 \qquad \phi_2 = \pi/6 \qquad \phi_3 = \pi/9$$

$$\phi_4 = \pi/12 \qquad \phi_5 = \pi/16$$

Parameters of feltmetal coating are the same as those used by Fedorov et al. [10], i.e.,

$$\phi = 0.75 \qquad h^* = 0.75\,\text{mm} \qquad \sigma^* = 1.66\times10^5\ \text{kg(m}^2\text{s}^{-1}\text{)}$$

$$a_\infty = 1 \qquad d^* = 30\mu\,\text{m} \qquad \gamma = 1.4$$

where the fiber diameter (d^*) is related to the characteristic pore size as follows,

$$r_p^* = \frac{\pi d^*}{2 - 3\phi + \phi^2} \tag{72}$$

Figures 4 to 5 compare pressure perturbation amplitude along the flat plate for the six cases of stability simulation. These three figures clearly show show that the two types of

porous coatings both destabilize mode S in Mack's first mode region and stabilize it in Mack's second mode region. For pure mode S propagating downstream, the overall effect of porous coating is destabilizing. At approximately the same porosity, regular porous coating is weaker in first-mode destabilization and second-mode stabilization than felt-metal porous coating. For regular porous coating, the results also show that porosity decreasing leads to even weaker first-mode destabilization and second-mode stabilization.

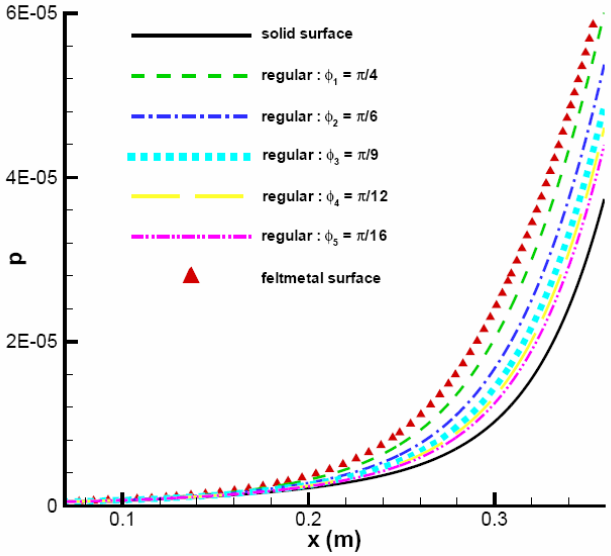

Fig. 4. Pressure perturbation amplitude along the flat plate for the six cases of stability simulations in Mack's first mode region.

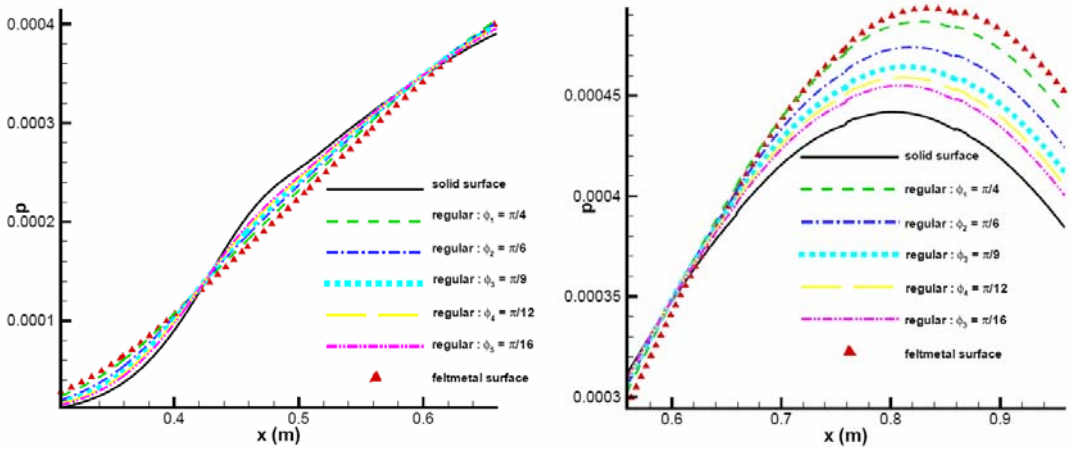

Fig. 5. Pressure perturbation amplitude along the flat plate for the six cases of stability simulations in Mack's second mode region.

We have also studied the effect of the phase angle of regular coating admittance for the coating with $\phi_1 = \pi/4$. Figure 6(a) shows the instantaneous pressure and velocity perturbations along the flat plate with regular porous coating at the given parameters. The amplitude of wall-normal velocity perturbation is proportional to that of pressure perturbation. It is also noticed that there is a phase discrepancy between the pressure and velocity perturbations, which is determined by the phase angle of porous coating admittance. Therefore, the effects of regular porous coating on mode S instability depend on the magnitude and phase angle of admittance simultaneously.

According to the model of porous coating, admittance magnitude only affects the amplitude of velocity oscillation. As a result, it will only affect the magnitudes of Mack's first mode destabilization and Mack's second mode stabilization. However, it will not affect the destabilization/stabilization behavior.

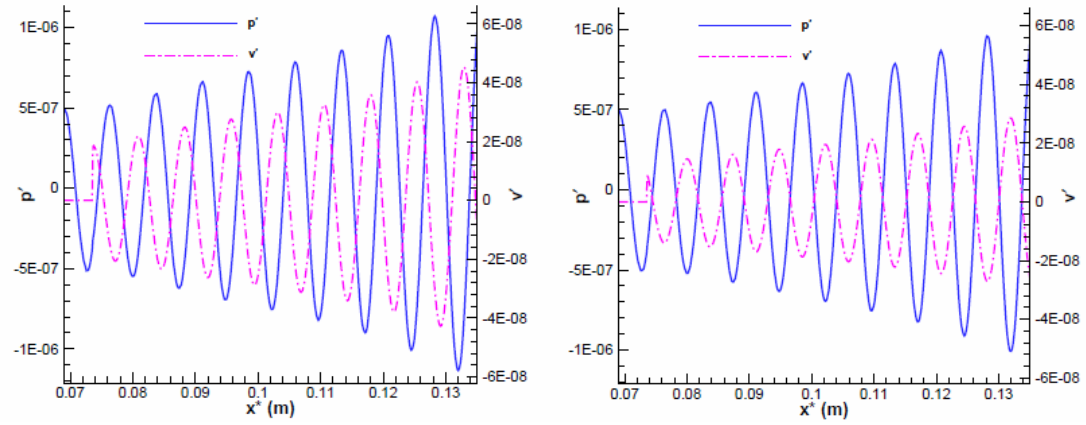

(a) at the given parameters *(b) zero imaginary part of admittance*

Fig. 6. Instantaneous pressure and velocity perturbations along the flat plate with regular porous coating.

To verify that the destabilization/stabilization behavior of porous coating is affected by the phase angle of admittance, we carried out numerical simulation on one "artificial" porous coatings with zero imaginary part of admittance (phase angle = π). The corresponding results are plotted as Fig. 6(b). The two plots in Fig. 6 clearly show the change of phase angle with the peak of velocity perturbation moving upstream. Figure 7 compares the pressure perturbation amplitudes for the two regular porous coatings, together with the spatial development of mode S along solid wall. The figure shows that pressure perturbation amplitude decreases with the phase angle of admittance decreasing. Since the synchronization point is located around x = 0.33 m, the results indicate that Mack's first mode destabilization is weakened by the decrease of admittance phase angle. However, the second mode stabilization is approximately unchanged because the pressure perturbations of two porous coatings increase proportionally after the synchronization point.

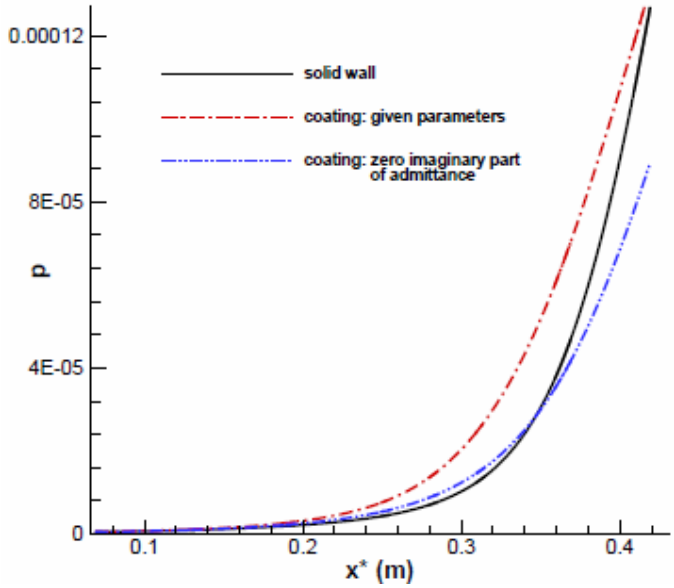

Fig. 7. Comparison of pressure perturbations for the two cases of regular porous coatings.

For real regular porous coating, we further analyze the admittance of porous coating. According to the model of regular coating, the admittance phase angle depends on three parameters: thickness, pore size, and ratio of specific heat. Figure 8 shows phase angle of admittance versus the three parameters, respectively, with the other parameters of porous coating unchanging. Figure 8(c) shows that phase angle decreases with the ratio of specific heat increasing, which again indicates that the effects of thermochemical non-equilibrium flow will lead to weaker destabilization of Mack's first mode.

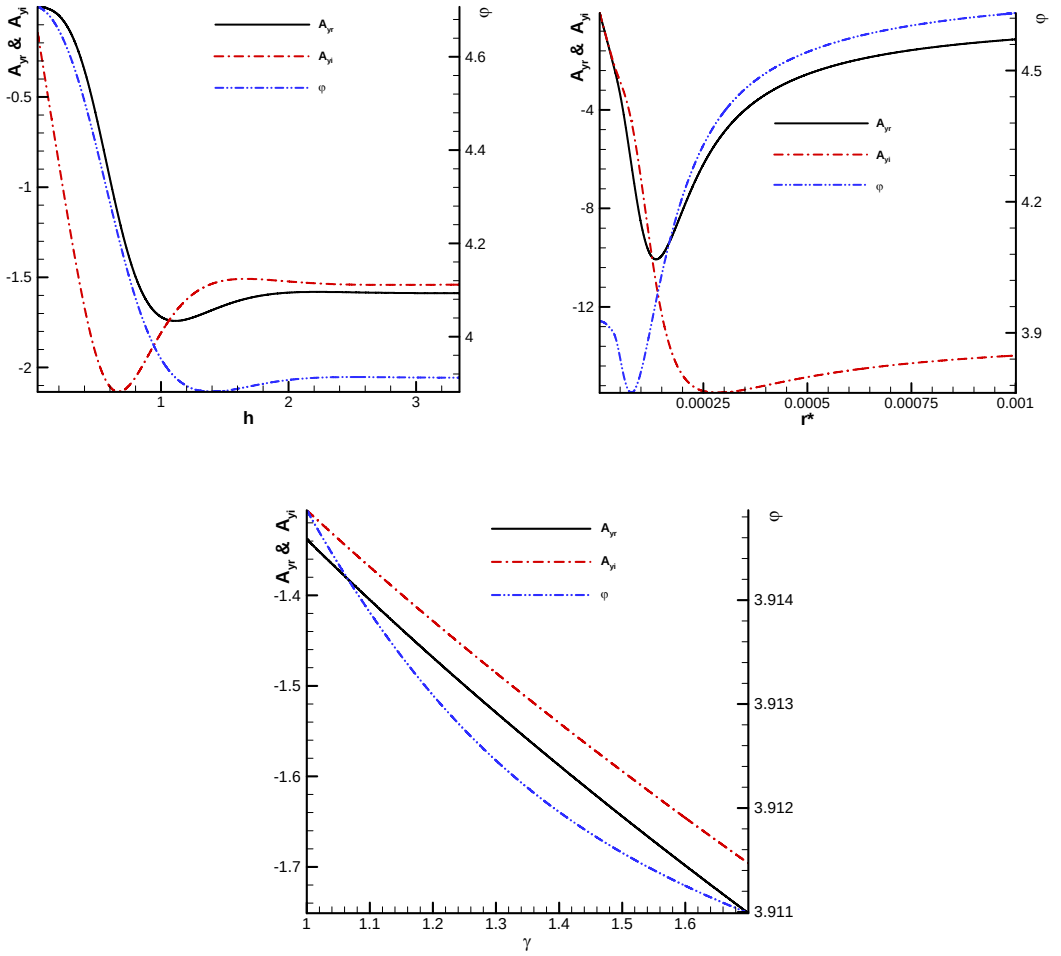

Fig. 8. Phase angle of regular porous coating admittance versus: thickness, pore size, and the ratio of specific heat.

In Figs. 8 for pore size and specific heat ratio, there is a minimum phase angle, which indicates there is optimal thickness and pore size. This minimum is helpful for the design of new porous coating. Since the decrease of phase angle is more significant for pore size, we try to design new porous coating based on pore size. Figure 8 for pore size shows that the minimum phase angle is achieved with the pore size being 77e− 6 m. Since a smaller phase angle leads to weaker first mode destabilization, we carried out numerical simulation on the new pore size, with other parameters of the porous coating keeping the same. Figure 9 shows the numerical results for the new porous coatings. The phase angle of admittance does decrease with the peak of velocity perturbation moving upstream.

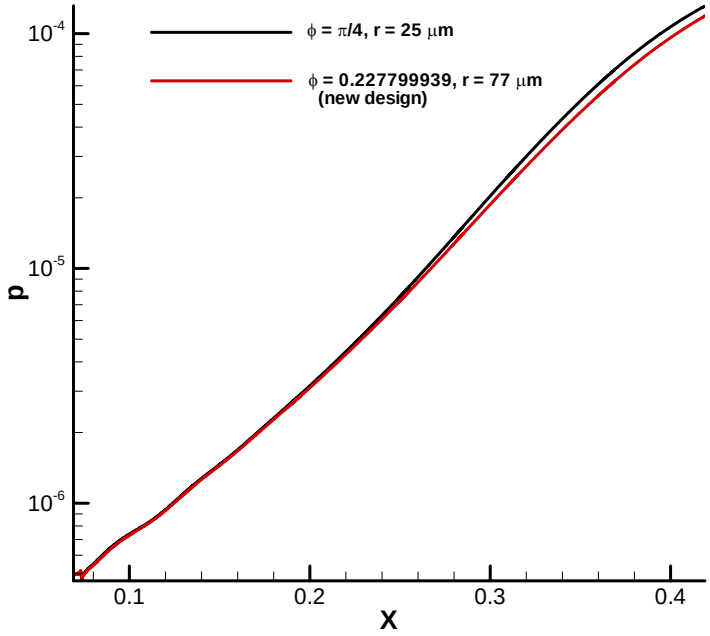

Fig. 9. Pressure perturbation amplitudes of the new designed porous coating and the origin one.

Based on the results for perfect gas flow, it is realized that numerical simulations based on perfect gas flow may not be enough. The effects of thermochemical non-equilibrium flow including internal energy excitations, translation-vibration energy relaxation, and chemical reactions among different species need to be considered. It is due to not only the effect of specific heat ratio on first-mode destabilization but the change of boundary-layer stability characteristics.

5. Test of shock-fitting method and non-equilibrium models

To consider the thermochemical non-equilibrium effects on the passive control of hypersonic boundary-layer transition using regular porous coating, a new high-order shock-fitting solver for non-equilibrium flow simulations has been developed based on 5-species air chemistry and recently non-equilibrium models. The code is based on a two-temperature model: translational and rotational energy modes are in equilibrium at the translational temperature whereas vibration energy, electronic energy, and free electron energy are in equilibrium at the vibration temperature. Here we focus our tests on shock-fitting method and thermochemical models.

5.1 Gnoffo's air dissociation over 1 meter radius cylinder

Figure 10 shows the mesh and flow conditions of the test case: 5-species air over a 1-meter radius cylinder. The temperatures on the cylinder are equal to Tw (= 500 K). Catalytic boundary conditions are applied on the wall for species mass fraction. Total density is computed from pressure and translational temperature. Then species densities are calculated with total density and mass fraction. Total energy and vibration energy are calculated using species densities and two temperatures. The mass fractions of initial gas are as follows,

$$C_{N2} = 0.76 \qquad C_{O2} = 0.24 \qquad C_{NO} = C_N = C_O = 0$$

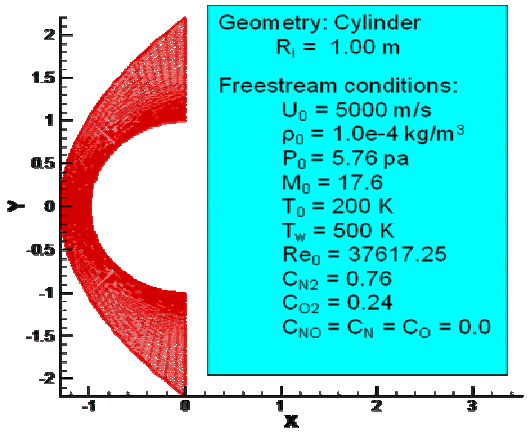

Fig. 10. Mesh sturcture and flow conditions of the test case.

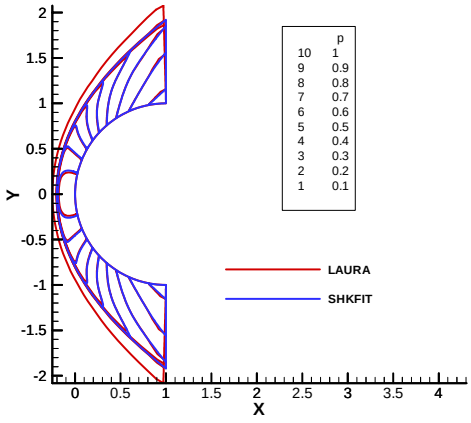

(a) Pressure

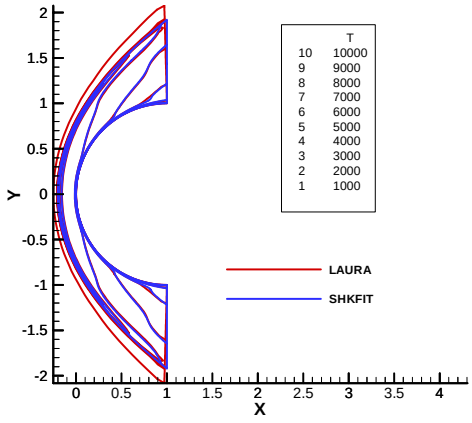

(b) Translation temperature

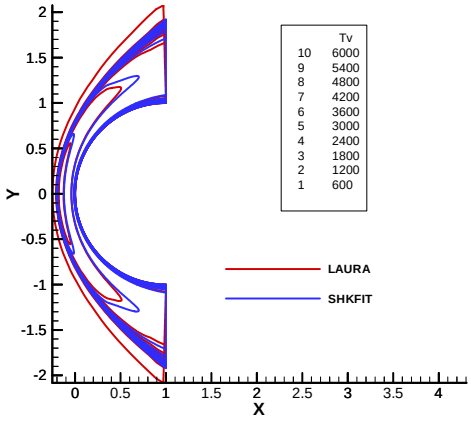

(c) Vibration temperature

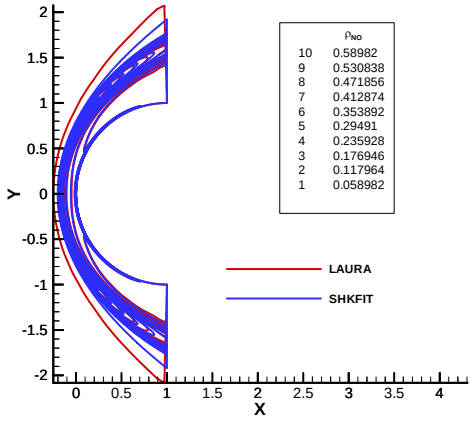

(d) Species density of NO

Fig. 11. Comparisons of flow field contours obtained from shock-fitting code with those obtained from Laura simulation.

To make the results comparable, flow conditions are exactly the same as what Gnoffo used in his simulation. The simulation results are compared with Gnoffo's results obtained from Laura. Figure 11 compares flow field contours obtained from current shock-fitting code with those obtained from Laura code. From the contours of pressure, temperatures, and NO density, it is found that shock standoff distances of the two sets of simulations have a good agreement. In addition, the flow fields near the wall have a good agreement. Near the shock, there is small discrepancy between the two sets of solution, mainly due to the different treatment of shock wave. Unlike the shock-fitting code, shock-capturing TVD scheme is applied in Laura code. Figure 11(c) shows that the vibration temperature of shock-fitting solution is significant different from that of Laura in the shock layer, which is mainly caused by the different models of vibration and electronic energy. Laura code used curved fitted vibration and electronic energy [21], whereas we used separate models for vibration energy and electronic energy.

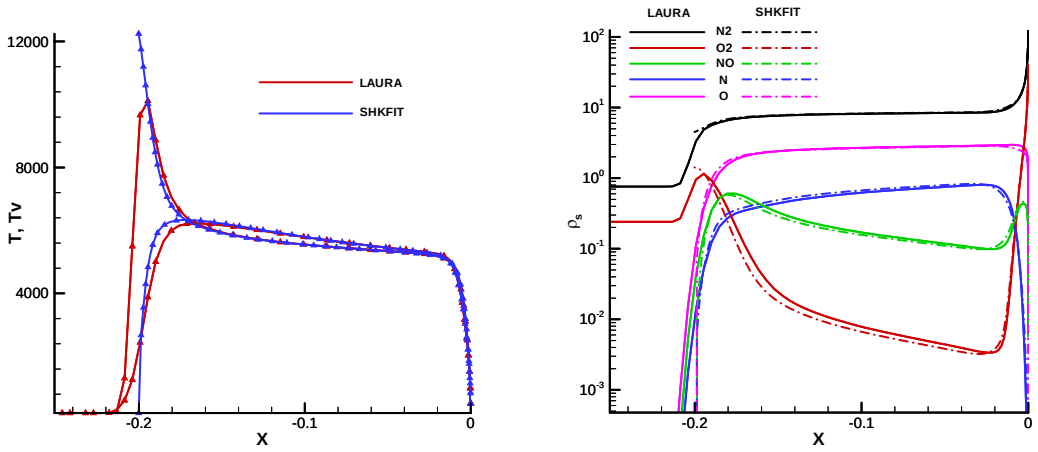

(a) Temperatures *(b) Species densities*

Fig. 12. Comparisons of flow variables along the stagnation line obtained from shock-fitting code with those obtained from Laura simulation.

Since we have detailed flow field information obtained from the Laura code, we can also compare the distributions of flow variables along the stagnation line or along the cylinder surface. For example, figure 12 compares flow variables along the stagnation line obtained from current shock-fitting code with those obtained from Laura code. These two figures also show that shock standoff distances of the two sets of simulations have a good agreement considering the different treatment of the bow shock. The distributions of temperatures and species densities along the stagnation line have a good agreement near the wall and have small discrepancy near the shock. Again, the discrepancy near the shock is due to the different treatment of shock wave. Overall, Figures 11 and 12 indicate that our shock-fitting non-equilibrium flow solver is reliable for the simulation of strong shock and turbulence interaction.

5.2 A Mach 10 flat-plate boundary layer with thermal equilibrium

The test case is got from Hudson's thesis [27]. The flow conditions of the flat-plate boundary layer are as follows,

$$M = 10 \qquad T_\infty = 278\text{K} \qquad p_\infty = 0.045\,\text{atm} \qquad u_\infty = 3351\,\text{m/s}$$

$$\rho_\infty = 0.0568\,\text{kg/m}^3 \qquad \text{Re}_\infty = 9.8425\times10^6/\text{m}$$

$$C_{N2} = 0.78 \qquad C_{O2} = 0.22 \qquad C_{NO} = C_N = C_O = 0$$

Our numerical results are compared with Hudson's theoretical solution and a recent boundary-layer solution from Prof. Tumin in Unversity of Arizona. Specifically, the temperature and velocity profiles across the boundary layer at x = 0.4 m are compared.

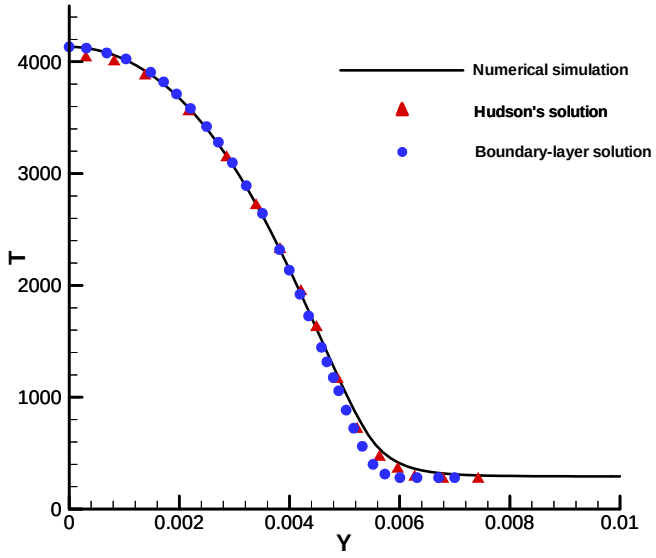

Fig. 13. Comparisons of temperature profiles across the boundary layer.

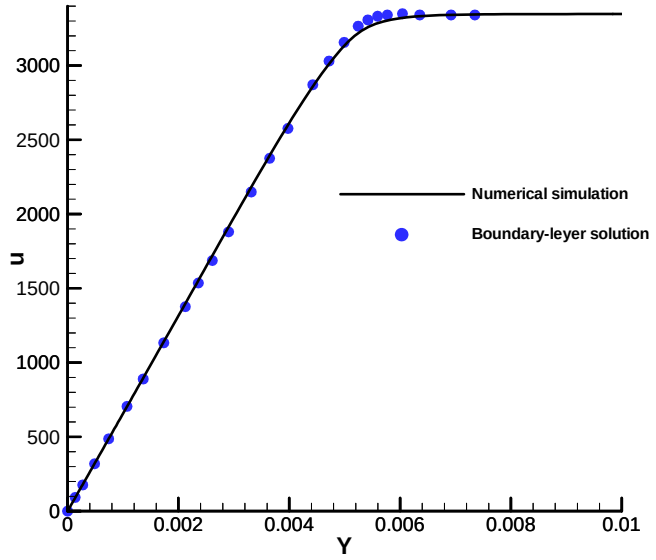

Fig. 14. Comparisons of streamwise velocity profiles across the boundary layer.

Figures 13 and 14 shows that the boundary-layer profiles obtained from our simulation have agreement with the theoretical solutions of Hudson and Tumin. The results indicate that our shock-fitting non-equilibrium flow solver is reliable.

6. Stabilization of a Mach 12.56 boundary layer over a blunted wedge

For practical thermal protection systems of hypersonic vehicles and re-entry vehicles, the ambient flows generally have a high Mach number and a pretty high enthalpy. Since thermochemical non-equilibrium effects are not significant in the Mach 5.92 flat-plate boundary layer due to low temperature, we have applied the high-order shock-fitting non-equilibrium solver to a Mach 12.56 flow over a blunted wedge of a half angle of 20 degree.

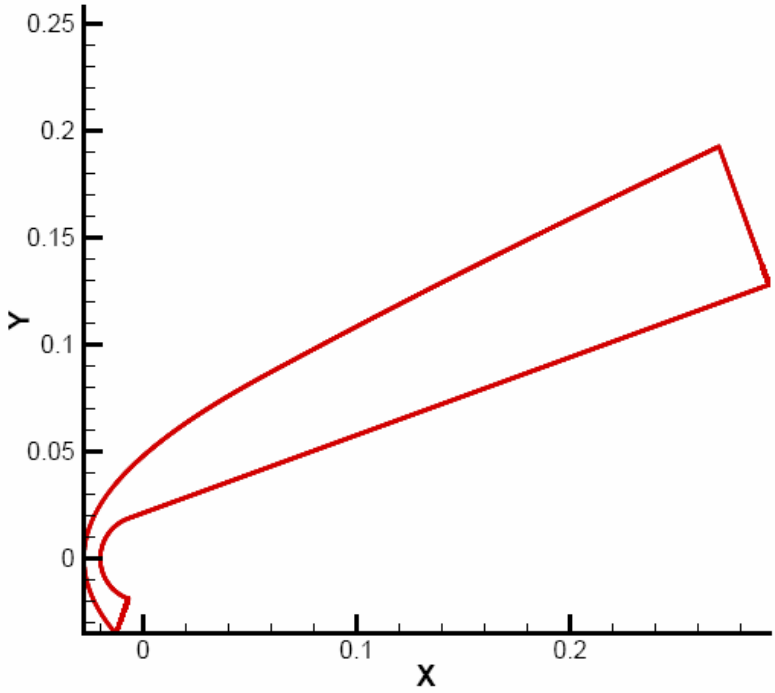

Fig. 15. A schematic of a Mach 12.56 flow over a blunted wedge.

Figure 15 shows a schematic of the Mach 12.56 non-equilibrium flow over a blunted wedge. The radius of the blunted leading edge is 2 cm. In Fig. 15, the lower boundary stands for the wedge surface whereas the upper boundary stands of the bow shock. The simulations of the Mach 12.56 flow are carried out with the isothermal condition. The specific flow conditions are as follows,

$$M_\infty = 12.56 \qquad p_\infty = 119.49\,\text{Pa} \qquad \rho_\infty = 1.45\times10^{-3}\,\text{kg}/\text{m}^3$$
$$T_w = 500\,\text{K} \qquad U_\infty = 4267.20\,\text{m/s} \qquad H_\infty \approx 9.4\,\text{MJ/kg}$$
$$c_{N_2} = 0.767 \qquad c_{O_2} = 0.233 \qquad c_{NO} = c_N = c_O = 0$$

It is noticed from the governing equations for perfect gas flow and non-equilibrium flow that transport properties are calculated based on different models. For example, the viscosity is computed by using Sutherland's law for perfect gas flow. But it is computed through evaluations of collision cross-section area. The difference of viscosity may significantly change in Reynolds number and the stability characteristics of the boundary layer. In the current problem, united Reynolds number is $347707.28/\text{m}$ for perfect gas flow and $328673.67/\text{m}$ for non-equilibrium flow. The effects of different viscosity are taken into account in the current paper by conducting three cases of numerical simulation: 1) perfect gas flow, 2) perfect gas flow with the transport properties being calculated from collision cross-section area, and 3) non-equilibrium flow.

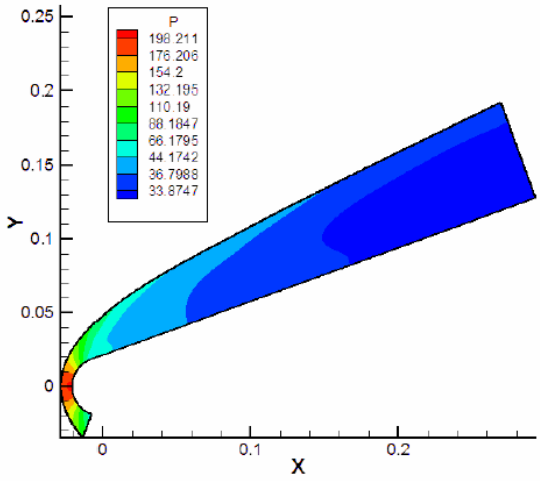

Case 1

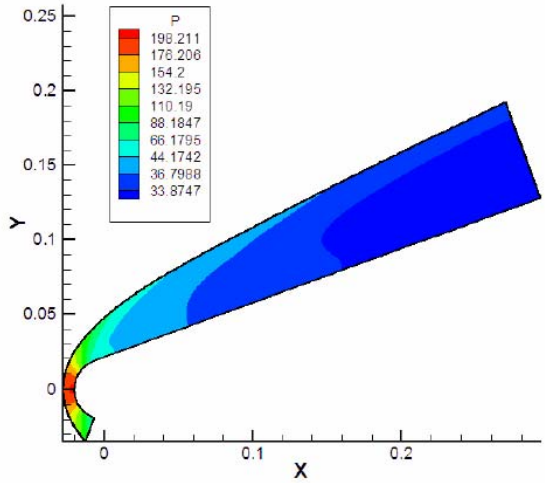

Case 2

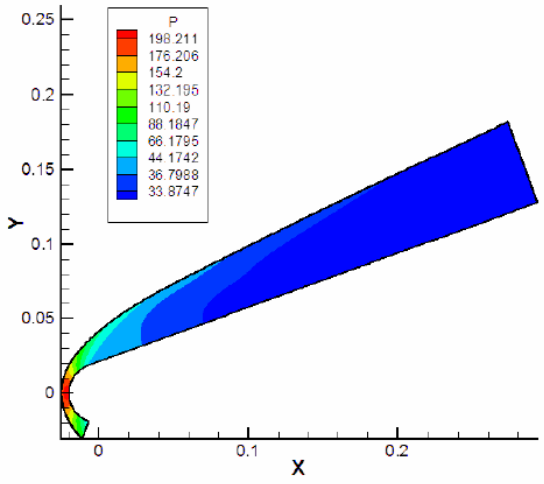

Case 3

Fig. 16. Pressure contours near the leading edge obtained from three cases of simulations.

Figure 16 compares the pressure contours near the leading edge obtained from three cases of numerical simulations. Here the geometry and levels of pressure are the same. The figures show that pressure contours of case 1 and case 2 are quite similar, and they are different from those of case 3. In addition, the shock standoff distance of non-equilibrium flow is much smaller than that of perfect gas flows due to chemical reactions and energy relaxation (more clear in Fig. 17).

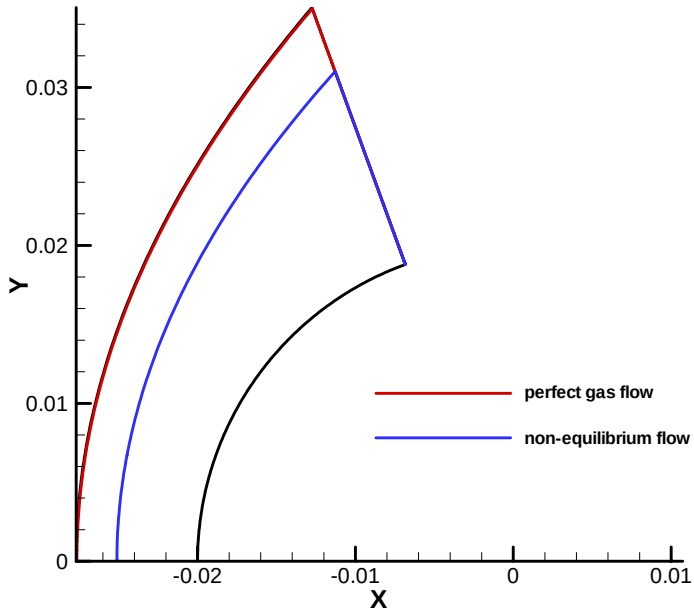

Fig. 17. Comparison of shock standoff distance.

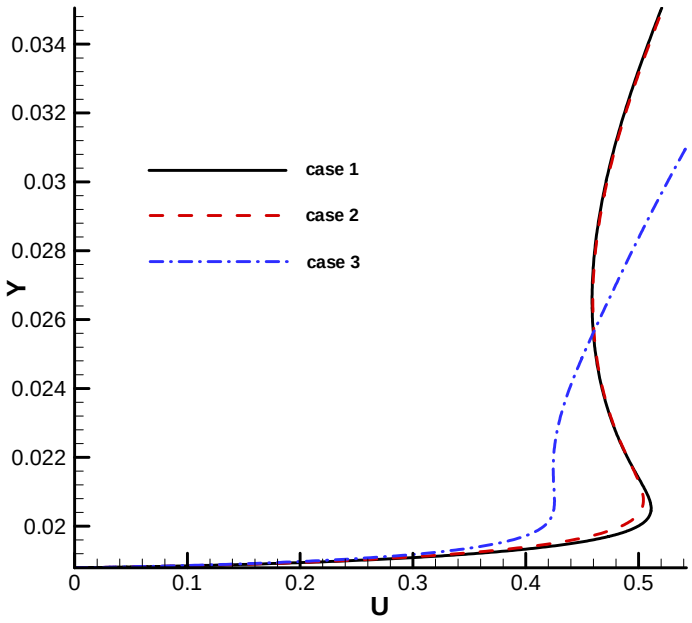

Fig. 18. Comparison of streamwise velocity profile across the boundary laye.

Figure 18 shows the streamwise velocity profile across the boundary layer at the intersection of the blunted leading edge and the wedge. The boundary layer of case 2 is a little bit thicker than that of case 1, because unit Reynolds number of perfect gas flow calculated from collision cross-section area is lower than that calculated from Sutherland's law. In addition, the boundary layer of case 3 is thinner than that of case 2. The results show that the effects of non-equilibrium flow and viscosity can be successfully separated by conducting the three cases of numerical simulations.

5. Summary

In current paper, we carried out numerical simulations on the passive control of hypersonic boundary-layer transition using regular porous coating. The stabilization of a Mach 5.92 flat-plate boundary layer by using regular coating is first studied for perfect gas flow. The results show that, at approximately the same porosity, regular coating is weaker in first-mode destabilization and second-mode stabilization than felt-metal coating. The porosity decrease of regular coating leads to even weaker first-mode destabilization and second-mode stabilization. The results also show that the first-mode destabilization decreases as the phase angle of admittance decreases and the thermochemical non-equilibrium of hypersonic flows may affect the stabilization efficiency of regular coating. Therefore, numerical simulations based on perfect gas flow may not be enough. The effects of thermochemical non-equilibrium flow including internal energy excitations, translation-vibration energy relaxation, and chemical reactions among different species need to be considered.

A high-order shock-fitting non-equilibrium flow solver based on 5-species air chemistry and recent thermal property models is applied to DNS of strong shock and turbulence interactions. The code is implemented based on a two-temperature model. It is assumed that translational and rotational energy modes are in equilibrium at the translational temperature whereas vibration energy, electronic energy, and free electron energy are in equilibrium at the vibration temperature. The code package has been validated.

The high-order non-equilibrium solver is being applied to numerical simulation of a Mach 12.56 boundary layer over a blunted wedge of 20 degree. Thermochemical non-equilibrium effects of hypersonic flows on the steady base flow are investigated by comparing numerical results of perfect gas flows and thermochemical non-equilibrium flow. Unsteady simulations on the passive control of hypersonic non-equilibrium boundary-layer transition using regular porous coating are currently ongoing.

Acknowledgments

This work was sponsored by the AFOSR/NASA National Center for Hypersonic Research in Laminar-Turbulent Transition and by the Air Force Office of Scientific Research, USAF, under Grants No. FA9550-07-1-0414 and FA9550-04-1-0029, monitored by Dr. John Schmisseur. The views and conclusions contained herein are those of the authors and should not be interpreted as necessarily representing the official policies or endorsements either expressed or implied, of the Air Force Office of Scientific Research, the National Aeronautics and Space Administration, or the U.S. Government.

Reference

1. *Report of the Defense Science Board Task Force on National Aero-Space Plane (NASP) Program*. 1992, Defense Science Board.
2. Zhong, X., and Wang, X., *Direct Numerical Simulation on the Receptivity, Instability, and Transition of Hypersonic Boundary Layers.* Annual Review of Fluid Mechanics, 2012. **44**: p. 527-561.
3. Reshotko, E., *Is Re_θ/Me a meaningful transition criterion ?* . AIAA Journal, 2007. **45**(7): p. 1441-1443.
4. Fedorov, A.V., and Tumin, A. , *High-Speed Boundary-Layer Instability: Old Terminology and a New Framework.* AIAA Journal, 2011. **49**(8): p. 1647-1657.
5. Mack, L.M., *Linear Stability Thoery and the Problem of Supersonic Boundary-Layer Transition.* AIAA Journal, 1975. **13**(3): p. 278-289.
6. Fedorov, A.V., Malmuth, N. D., Rasheed, A., and Hornung, H. G., *Stabilization of hypersonic boundary layers by porous coatings.* AIAA Journal, 2001. **39**(4): p. 605-610.
7. Chokani, N., Bountin, D. A., Shiplyuk, A. N., and Maslov, A. A., *Nonlinear aspects of hypersonic boundary-layer stability on a porous surface.* AIAA Journal, 2005. **43**(1): p. 149-155.
8. Fedorov, A.V., and Malmuth, N. D., *Parametric studies of hypersonic laminar flow control using a porous coating of regular microstructure.* AIAA Paper 2008-588, 2008. .
9. Rasheed, A., Hornung, H. G., Fedorov, A. V., and Malmuth, N. D., *Experiments on passive hypervelocity boundary-layer control using an ultrasonically absorptive surface.* AIAA Journal, 2002. **40**(3): p. 481-489.
10. Fedorov, A.V., Shiplyuk, A. N., Maslov, A. A., Burov, E. V., and Malmuth, N. D., *Stabilization of a hypersonic boundary layer using an ultrasonically absorptive coating.* Journal of Fluid Mechanics, 2003. **479**: p. 99-124.
11. Shiplyuk, A.N., Burov, E. V., Maslov, A. A., and Fomin, V. M., *Effect of porous coatings on stability of hypersonic boundary layers.* Journal of Applied Mechanics and Technical Physics, 2004. **45**(2): p. 286-291.
12. Fedorov, A.V., Kozlov, V. F., Shiplyuk, A. N., Maslov, A. A., and Malmuth, N. D., *Stability of hypersonic boundary layer on porous wall with regular microstructure.* AIAA Journal, 2006. **44**(8): p. 1866-1871.
13. Maslov, A.A., *Stabilization of Hypersonic Boundary Layer by Microstructural Porous Coating.* IUTAM Symposium on One Hundred Years of Boundary Layer Research, 2006.
14. Lukashevich, S.V., Maslov, A. A., Shiplyuk, A. N., Fedorov, A. V., and Soudakov, V. G., *Stabilization of high-speed boundary layer using porous coating of various thickness.* AIAA Paper 2010-4720, 2010.
15. Bres, G.A., and Colonius, T., *Three-dimensional instabilities in compressible flow over open cavities.* Journal of Fluid Mechanics, 2008. **599**: p. 309-339.
16. Egorov, I.V., Fedorov, A. V., and Soudakov, V. G., *Receptivity of a hypersonic boundary layer over a flat plate with a porous coating.* Journal of Fluid Mechanics, 2008. **601**: p. 165-187.
17. Sandham, N.D., and Ludeke, H., *Numerical study of Mach 6 boundary-layer stabilization by means of a porous surface.* AIAA Journal, 2009. **47**(9): p. 2243-2252.
18. Wang, X., and Zhong, X., *Effect of porous coating on boundary-layer instability.* AIAA Paper 2010-1243, 2010.
19. Wang, X., and Zhong, X., *Numerical Simulations on mode S growth over feltmetal and regular porous coatings of a Mach 5.92 flow.* AIAA Paper 2011-375, 2011.
20. Hash, D., Olejniczak, J, Wright, M. J., Dinish, P., Pulsonetti, M., Hollis, B. R., Gnoffo, P. A., Barnhard, M., Nompelis, I., and Candler, G., *FIRE II Calculations for Hypersonic*

Nonequilibrium Aerothermodynamics Code Validation: DPLR, LAURA, and US3D. 2007, AIAA 2007-0605.
21. Gnoffo, P.A., Gupta, R. N., and Shinn, J. L., *Conservation equations and physical models for hypersonic air flows in thermal and chemical nonequilibrium*. 1989, NASA Technical Paper 2867.
22. Candler, G.V., *The computation of weakly ionized hypersonic flows in thermo-chemical nonequilibrium*. 1988, Stanford University.
23. Gupta, R.N., Yos, J. M., Thompson, R. A., and Lee, K-P., *A Review of Reaction Rates and Thermodynamic and Transport Properties for an 11-Species Air Model for Chemical and Thermal Nonequilibrium Calculations to 30 000 K*. 1990, NASA Reference Publication 1232.
24. Park, C., *Nonequilibrium hypersonic aerothermodynamics*. 1990, New York: Wiley. .
25. Zhong, X., *High-order finite-difference schemes for numerical simulation of hypersonic boundary-layer transition.* Journal of Computational Physics, 1998. **144**: p. 662-709.
26. Allard, J.-F., and Champoux Y., *New empirical equations for sound propagation in rigid frame fibrous materials.* The Journal of the Acoustical Society of America, 1992. **91**(6): p. 3346-3353.
27. Hudson, M.L., *Linear Stability of Hypersonic Flows in Thermal and Chemical Nonequilibrium*. 1996, North Carolina State University.